Nanotechnology

Hyperbranched TiO_2-CdS Nano-Heterostructures for Highly Efficient Photoelectrochemical Photoanodes

To cite this article before publication: Alessandro Mezzetti *et al* 2018 *Nanotechnology* in press https://doi.org/10.1088/1361-6528/aac852

Hyperbranched TiO_2-CdS Nano-Heterostructures for Highly Efficient Photoelectrochemical Photoanodes

Alessandro Mezzetti,[a, †] Mehrdad Balandeh,[a, †] Jingshan Luo,[b] Sebastiano Bellani,[a] Alessandra Tacca,[c] Giorgio Divitini,[d] Chuanwei Cheng,[e] Caterina Ducati,[d] Laura Meda,[c] Hongjin Fan[b] and Fabio Di Fonzo[a, *]

a - Center for Nano Science and Technology, Istituto Italiano di Tecnologia, Milano, Italy.

b - School of Physical and Mathematical Sciences, Nanyang Technological University, Singapore, Singapore.

c - Centro Ricerche per le Energie Non Convenzionali, Istituto ENI Donegani, Novara, Italy.

d - Department of Materials Science & Metallurgy, University of Cambridge, Cambridge, UK.

e - Shanghai Key Laboratory of Special Artificial Microstructure Materials and Technology, Tongji University, Shanghai, China

† - These authors contributed equally to this work.

* - Corresponding author: fabio.difonzo@iit.it

Abstract

Quasi-1D hyperbranched TiO_2 nanostructures are grown via pulsed laser deposition and sensitized with thin layers of CdS to act as a highly efficient photoelectrochemical photoanode. The device properties are systematically investigated by optimizing the height of TiO_2 scaffold structure and thickness of the CdS sensitizing layer, achieving photocurrent values up to 6.6 $mA \cdot cm^{-2}$ and reaching saturation with applied biases as low as 0.35 V_{RHE}. The high internal conversion efficiency of these devices is to be found in the efficient charge generation and injection of the thin CdS photoactive film and in the enhanced charge transport properties of the hyperbranched TiO_2 scaffold. Hence, the proposed device represents a promising architecture for heterostructures capable of achieving high solar-to-hydrogen efficiency.

Introduction

Photoelectrochemical (PEC) water-splitting stands as a promising method to employ the clean energy of solar light as the driving force to extract hydrogen from aqueous solutions, using inexpensive metal oxide photoelectrodes as the working devices.[1] Since the discovery of the photocatalytic properties of TiO_2 made in 1972 by Honda and Fujishima,[2] research has focused its efforts to increase the efficiency of the materials used as photoelectrodes. Due to its low cost, easy availability and high chemical stability in both strongly acidic and basic environments, TiO_2 has been always considered an important material for applications in PEC water-splitting.[3–9] Initial studies on TiO_2 have dealt with the development of optimized nanostructures in order to improve the efficiency of photoelectrodes. Thin films made by metal oxide nanoparticles display an increased effective surface area compared to bulk structures, but suffers from low electron mobility due to electron trapping at grain boundaries.[10–15] Quasi-1D nanostructures like nanorods (NRs) and nanotubes (NTs) have been demonstrated to have enhanced electron mobility, although the reported efficiencies remain low due to their intrinsic limited surface area and low optical density.[16–21] Latest

researches are now focused towards the goal of high surface area quasi-1D hierarchical nanostructures that could benefit from both high surface area and enhanced electronic transport.[22–24]

Regardless of the nanostructure employed, the performances of a bare TiO_2 photoelectrode are limited by its wide band-gap of 3.2 eV, which restricts the photocatalytic activity to the near UV region (up to 385-390 nm of wavelength) and limits the resulting solar-to-hydrogen (STH) efficiency to a maximum theoretical value of approximately 2%. Various methods have been developed to shift the photoactivity threshold of TiO_2 towards the visible region of the solar spectrum, either by doping with other elements[25–33] or by sensitization with low band-gap absorber materials. Among the wide range of materials employed for the sensitization of TiO_2 scaffolds, cadmium sulfide (CdS) stands as a valid candidate thanks to its opto-electronic properties that satisfy the strict PEC requirements: the optical bandgap of 2.42 eV allows to absorb light in the visible range up to 510 nm and the conduction band and valence band are correctly aligned with respect of the hydrogen and oxygen evolution potentials respectively. On the downside, CdS suffers from low charge separation efficiency, leading to a strong photocorrosion in aqueous environment, as the photogenerated holes in the valence band oxidize the sulfide ions instead of water, releasing S2+ and Cd2- ions in the solution; experimentally, this drawback is fully countered with the addition of one or more sacrificial agents (usually Na2S and Na2SO3) into the electrolytic solution employed for the PEC measurements.[34] Furthermore, CdS is classified as a toxic material (NFPA 704 Class 3 health hazard) and thus limiting its viability for an eventual industrial scale-up. Nevertheless, CdS has been extensively studied as a prototypical absorber for TiO_2 sensitization, resulting in a substantial amount of publications spanning over the last years.[35–56] Among these works, different TiO_2 morphologies and different techniques for CdS sensitization are employed in the fabrication of PEC photoanodes, in order to find the optimal architecture in terms of charge generation, onset potential and overall conversion efficiency.

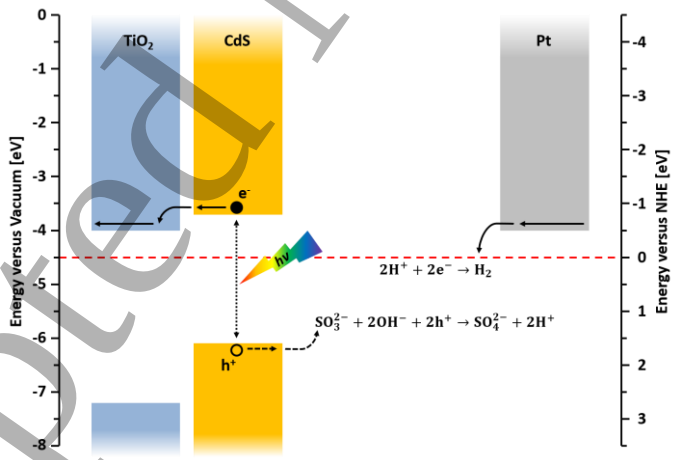

Figure 1 - Schematic of the energy band alignment of the PEC setup employing a TiO_2/CdS photoanode as the working electrode, showing the hydrogen evolution reaction occurring at the platinum dark cathode and the sulfides sacrificial reaction occurring at the TiO_2/CdS photoanode.

The concept behind this work is to develop a host/guest PEC photoanode comprising an optimized nanostructured metal oxide scaffold sensitized with a well-reported photoabsorber material, in order to properly compare and evaluate the effectiveness of the proposed structure. Tree-like hyperbranched TiO_2 nanostructured scaffolds are developed exploiting gas phase self-assembly using the pulsed laser deposition (PLD) technique, resulting in a high surface area scaffold with efficient light harvesting and

charge transport properties, as successfully employed in previous works.[57–60] To compensate for the limited absorption range of TiO_2, the nanostructured scaffolds are sensitized with a thin layer of CdS via chemical bath deposition (CBD), forming a type-II heterostructure (Figure 1) that favors the separation of photogenerated charges. Optimization of the resulting heterostructure is performed by varying both the thickness of the supporting hyperbranched scaffold and the amount of CdS deposited on the scaffold surface through the sensitization process. A thorough analysis is performed to assess the morphological, optical and electrochemical properties of the different photoanodes. At the end, a comparison with other architectures present in literature is presented, showing the improved performances that the hyperbranched TiO_2 scaffold provides to the whole photoanodic heterojunction.

Methods

Samples preparation

The TiO_2 nanostructures are deposited via pulsed laser deposition (PLD). Laser pulses from a KrF excimer laser (wavelength 248 nm, repetition rate 20 Hz, laser fluency of 2.5 $J \cdot cm^{-2}$) are employed to ablate a titanium dioxide (TiO_2) target placed within a vacuum chamber (standard vacuum in the order of 10^{-3} Pa) filled with O_2 background gas up to the desired working pressure. Briefly, laser pulses impinge upon the target, which is locally vaporized and partially ionized, generating a plasma that expands supersonically towards the substrate. The ablated species condense on the substrate and form a film, whose morphological characteristics can be controlled by varying the deposition parameters, such as background gas pressure, laser fluence and target to substrate distance. Each material has a precise processing window where it is possible to induce gas-phase nucleation of clusters. The nucleated clusters scatter upon interaction with the background gas molecules, resulting in the self-assembly of quasi-1D nanostructures with a typical diameter of hundreds of nanometers and with a height proportional to the deposition time. The films are deposited on 2.3-mm-thick soda-lime glasses slides coated with an FTO conductive coating (sheet resistance of 15 Ω/sq), properly etched to obtain a limited active area of 1.8 cm^2. All samples are deposited at room temperature, yielding amorphous films. The crystalline phase transition from the deposited amorphous phase is achieved through a post-deposition annealing treatment, performed in a muffle furnace in air for 2 hours at 500°C. As reported in previous works concerning quasi-1D TiO_2 nanostructures deposited via PLD, different background pressures yield TiO_2 film morphologies ranging from compact to extremely porous, with a small operational window where hyperbranched nanostructures are obtained. The range for hierarchical structures is found between 5 Pa and 20 Pa, with an optimal value of 7 Pa here employed to obtain the hyperbranched scaffolds. A reference device is fabricated using a TiO_2 nanoparticle paste, deposited on the same FTO-coated glass substrate using the Doctor Blade technique and calcinated through a thermal treatment in air for 30 minutes at 500 ˚C.

The sensitization technique – a specific type of chemical bath deposition called Successive Ionic Layer Absorption and Recombination (SILAR) – is employed to deposit a thin and homogeneous layer of CdS over the complex hierarchical structure of the TiO_2 scaffolds. The sensitization protocol consists in immersing the bare TiO_2 samples first in a 20 mM ethanol solution containing the cadmium chemical precursor (cadmium acetate dehydrate, $Cd(Ac)_2 \cdot 2H_2O$) for 90 seconds, in order to allow the Cd^{2+} ions to be adsorbed on the TiO_2 surface. The samples where then rinsed in pure ethanol and

dried with a nitrogen flux. The dried samples where successively immersed in a 20 mM methanol solution containing the sulfur chemical precursor (sodium sulfide nonahydrate, $Na_2S{\cdot}9H_2O$) for 90 seconds, so that the preadsorbed Cd^{2+} ions could react with the S^{2-} anions and form the desired CdS. As for the previous steps, the samples are rinsed in a pure methanol solution and dried with a nitrogen flux. All the aforementioned steps make up for a single cycle of the SILAR procedure, which can then be repeated subsequently in order to tailor the thickness of the deposited CdS film.

Samples characterization

Film morphology is investigated using a Field Emission Scanning Electron Microscope (Zeiss SUPRA 40) and a High-Resolution Transmission Electron Microscope (JEOL 4000EX with LaB6 filament operated at 400 kV accelerating voltage). Additional information on the crystallinity of the films is obtained through X-ray diffraction (Philips PW3020, Cu K_α radiation) and Raman spectroscopy (Renishaw InVia, excitation wavelength 532 nm) analyses.

The optical properties of the samples are probed with a UV/VIS spectrometer (Perkin Elmer Lambda 1050) operating with an integrating sphere. The absorptance is calculated from the experimental transmittance and reflectance data with the following formula:

$$A = 100 - T - R$$

where *A* is the absorptance, *T* is the transmittance and *R* is the reflectance.

Linear sweep voltammetry (LSV) measurements are carried out using a potentiostat/galvanostat (Autolab PGSTAT30) with a scan rate of 20 mV/s in a 3-electrodes configuration, with a TiO_2/CdS sample as the working electrode, a platinum wire (surface area of 0.8 mm^2) as the counter electrode and Ag/AgCl in saturated KCl as the reference electrode. The electrolyte is an aqueous solution of 0.25 M $Na_2S \cdot 9H_2O$ and 0.35 M Na_2SO_3 with a measured pH of 12.4. The illumination source is a Class AAA solar simulator (Oriel Model 94063A with solar filter) that simulates the AM 1.5G solar spectrum with a calibrated intensity of 100 $mW{\cdot}cm^{-2}$.

Incident-photon-to-current efficiency (IPCE) curves are obtained using the same 3-electrodes configuration, with the illumination source being a 150 W Xenon lamp coupled to a monochromator (Oriel Cornerstone 130); the photocurrent signal is recorded with the potentiostat/galvanostat (Autolab PGSTAT 30) and the incident irradiance is measured with a calibrated silicon photodiode (Centronic OSD 7Q). The measurements are performed with an applied bias of 0.2 V_{RHE}, corresponding to the maximum power point voltage of the devices obtained from the LSV curves. The IPCE values are then calculated in accordance to the following formula:

$$IPCE = 1.24 \times 10^3 \times \frac{J\left(\frac{\mu A}{cm^2}\right)}{\lambda(nm) \times P\left(\frac{W}{cm^2}\right)}$$

where *J* is the photocurrent density, λ is the wavelength of the incident light and *P* is the radiant power density at that given wavelength.

Electrochemical impedance spectroscopy (EIS) measurements are carried out with the same setup in a 2-electrode configuration (without the Ag/AgCl reference electrode) and without any illumination source.

Results and discussion

Materials characterization

Based on previous works that employed the PLD setup to deposit transition metal oxides, the operational parameters of the deposition are here optimized to obtain hyperbranched TiO_2 nanostructures. This distinctive tree-shaped morphology consists of a main stem perpendicular to the sample surface from which several branches develop, themselves having their own ramification and thus forming a complex hierarchical structure within a conical envelope of 15-20° with respect of the main growth axis, as can be appreciated from the SEM images of a TiO_2 sample (Figure 2a).

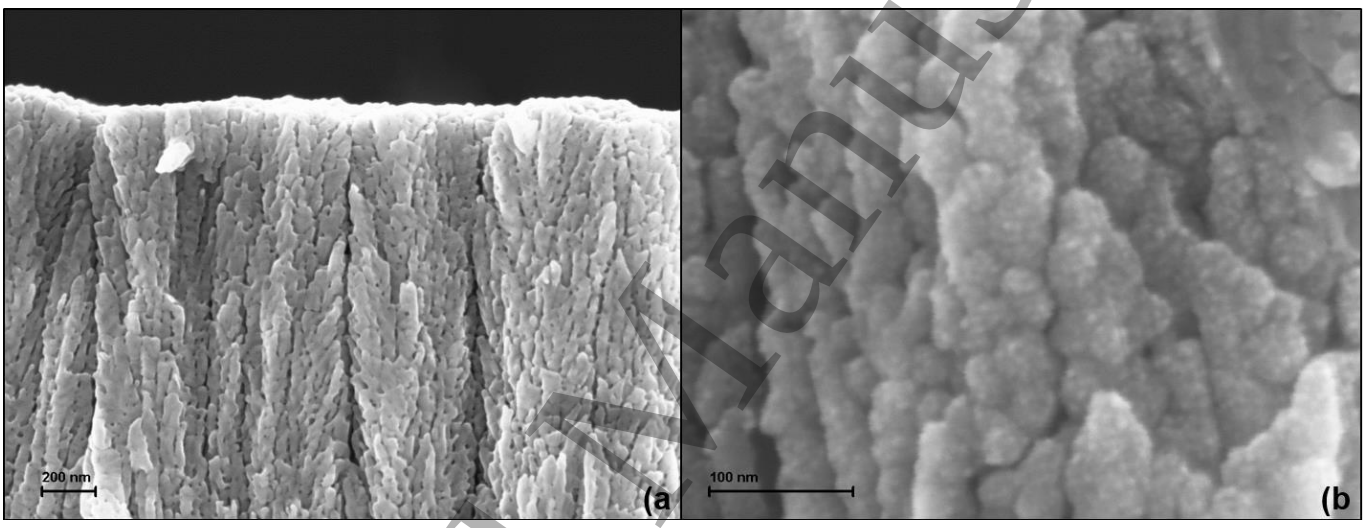

Figure 2 – Cross-sectional SEM image of the bare TiO_2 nano-tree morphology (a) and a close-up of the sensitized TiO_2/CdS heterostructure (b).

High resolution TEM images (Figure 3a and 3b) show well resolved lattice fringes of the TiO_2 branches even at their outer surface, thus confirming the high crystallinity of the tree-like nanostructure. The TEM diffraction spot pattern (Figure 3a Inset) suggests that the branches consist of single-crystalline tetragonal TiO2 in its Anatase phase, growing preferentially along the [001] direction.

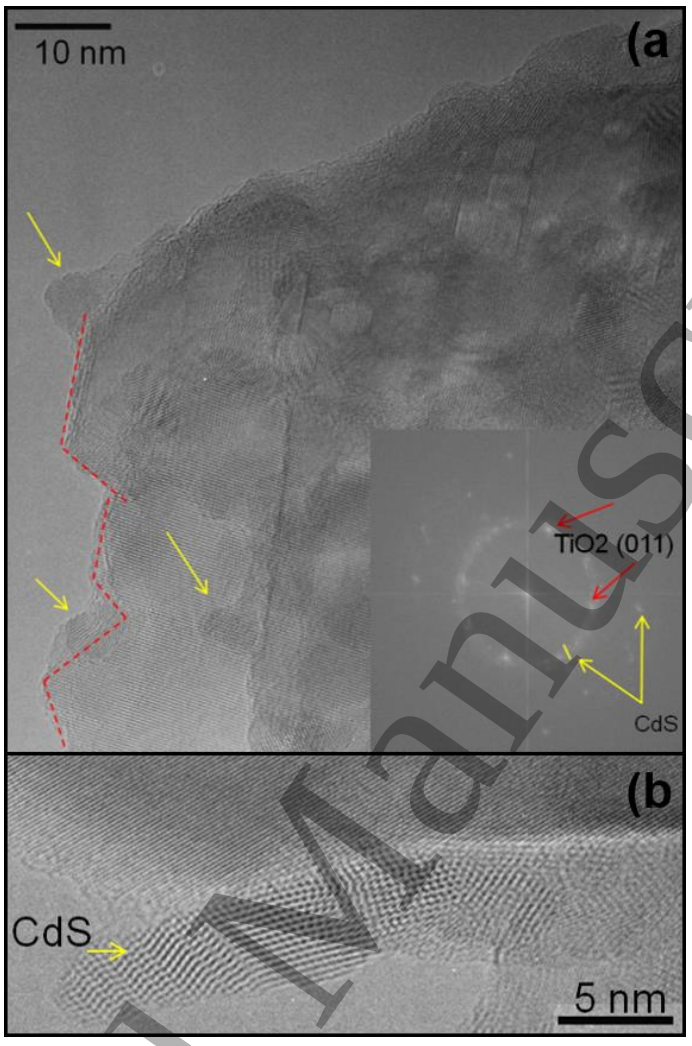

Figure 3 - High resolution TEM images of the TiO_2 nano-trees with the CdS layer in the sensitized heterostructure (a, b). The inset shows the Fast Fourier Transform of the lattice, where the main spacings are highlighted.

The preferential growth of the TiO_2 branches along the [001] direction (c-axis of the tetragonal crystalline structure of Anatase) is highlighted and confirmed by the X-ray diffraction spectra (Figure 4). The intensity ratio of the (004) peak at 37.8° with respect to the (101) peak at 25.3° has a value of 1.33 for the nanostructured TiO_2 and a value of 0.198 for the isotropic reference powder, almost a tenfold increase that clearly suggests a strong directionality during crystal growth.[24,59] This feature is also shared – with less intensity – by other diffraction peaks related to the growth partially along the c-axis, such as the (105) and (116) peaks. The confirmed single-crystal nature of the branches and directional growth of the nano-trees can be summarized in the hyperbranched character of the TiO_2 scaffold array.

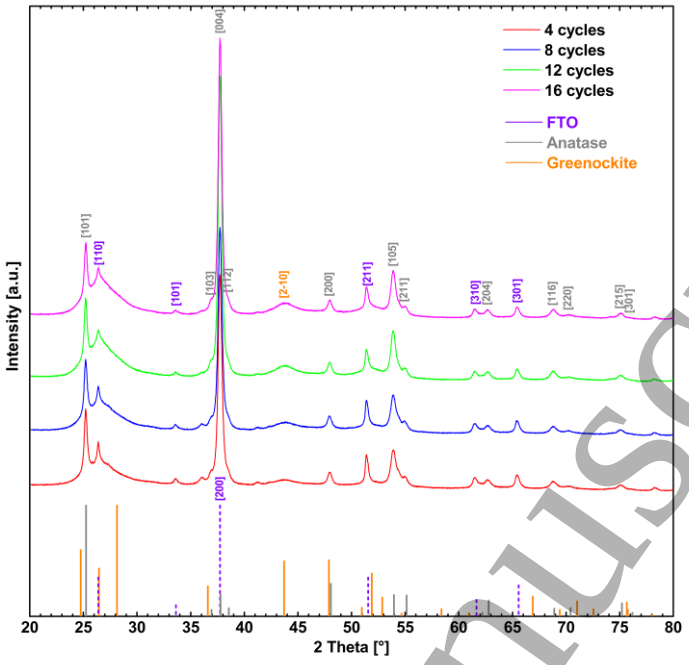

Figure 4 - XRD spectra of the 5-µm-thick TiO_2 scaffolds with increasing numbers of CdS sensitization cycles. The normalized peak patterns and the peak numbers for each reference crystalline phase are superimposed to the experimental data.

After being sensitized with few nanometers of CdS through a given amount of SILAR cycles, a homogenous coverage of the TiO_2 scaffold surface is achieved without any compromising effect on the porosity of the supporting nanostructure, as can be seen in the SEM and TEM images of a TiO_2/CdS sample (Figure 2b, 3a and 3b). Although mainly overshadowed by the contribution of the TiO_2 peaks, the XRD pattern of the sensitizing material is assigned to the hexagonal phase of CdS, the so-called Greenockite phase.[53] The intensity of the (2-10) diffraction peak of CdS – the only peak clearly distinguishable – increases with the number of SILAR cycles performed, as the amount of deposited CdS grows and leads to an increase in the signal intensity detected. The width of the crystallographic (2-10) peak is extremely broad when compared to the width of the TiO_2 peaks and is due to the homogeneous broadening caused by the nanometric dimensionality of the CdS grains, whose size has been calculated to be around 5 nm with Scherrer's equation. Both the thickness and morphology of CdS film are confirmed by the high resolution TEM images (Figure 3c and 3d), where an amorphous layer of CdS with small polycrystalline aggregates of approximately 5 nm in diameter covers homogenously the TiO_2 surface. The lattice spacing estimated for the CdS falls between 3.0-3.7 Å and their scattering pattern seems to indicate the presence of hexagonal or intermediate phases.

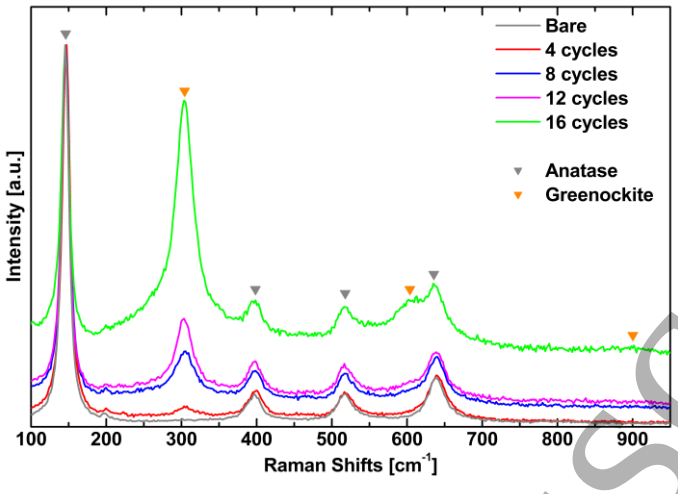

Figure 5 - Raman spectra of the 5-µm-thick TiO_2 scaffolds, both bare and with increasing numbers of CdS sensitization cycles. The colored arrows mark the peak for each crystalline phase.

As a further confirmation of the crystalline phases present in the film, Raman spectra of both bare TiO_2 and of TiO_2/CdS films are reported (Figure 5). The presence of TiO_2 in its tetragonal Anatase structure ($I4_1/amd$ space group) is confirmed by the presence of the peaks related to its vibration modes, at 145 cm^{-1} and 635 cm^{-1} for the E_g state, at 398 cm^{-1} for the B_{1g} state and at 516 cm^{-1} for the B_{1g} and A_{2g} states.[21,61] Superimposed on the strong signal of the crystalline TiO_2 scaffold there is the contribution of the CdS sensitizer in its hexagonal Greenockite structure ($P6_3mc$ space group), with the peaks related to the longitudinal optical (LO) phonon mode around 300 cm^{-1} for the fundamental first-order, around 600 cm^{-1} for the second-order overtone and around 900 cm^{-1} for the third-order overtone.[62–64] The intensity of the overtone peaks decreases by one order of magnitude each time, when compared to the first-order tone. Overall, the intensity of the three CdS peaks increases with the number of sensitization cycles, as more material is present in the scattering volume probed. The first-order LO phonon mode is present throughout all the sensitized samples, while the second-order peak starts as a shoulder of the well-defined 653 cm^{-1} Anatase peak and develops as the number of cycle increases. The third-order peak around 900 cm^{-1} is barely present in the spectrum of the 16-cycles sample, since the low yield of a third-order overtone can be faintly measured only with the highest amount of CdS scattering material.

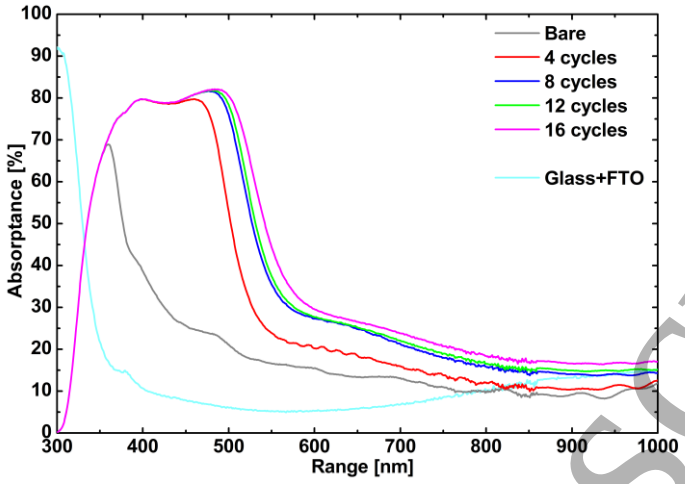

Figure 6 - Absorptance spectra of the 5-µm-thick TiO_2 scaffolds, both bare and with increasing numbers of CdS sensitization cycles. The spectra are shown without the absorptance contribution of the glass plus FTO substrate, which is also reported.

The optical properties of the deposited samples are assessed through UV-Vis spectrophotometry, shown in the form of absorptance (100-T-R) spectra for both the bare and sensitized samples (Figure 6). Since the optical measurements are performed by shining light on the glass side of the devices, the contribution of the TiO_2 or TiO_2/CdS film alone is obtained by subtracting the spectrum of a clean glass plus FTO from the experimental data. The bare TiO_2 scaffold presents an absorption value of 70% located in the near-UV region up to approximately 390 nm, in agreement with the Anatase bang-gap energy of 3.2 eV. On the other hand, sensitized samples show an absorption value of 80% in an extended range up to 510 nm, due to the CdS band-gap energy of approximately 2.4-2.5 eV. The value of the CdS band-gap energy - and thus the wavelength of the absorption cut-off - undergoes a red-shift in relation to the number of sensitization cycles, due to the quantum confinement effect related to the thickness of the sensitization layer. As the number of sensitization cycles increases, so does the thickness of the deposited CdS layer, reducing the quantum confinement on the optical band-gap and finally reaching its bulk-like value for the 1 cycles samples. The exact values of the optical band-gap for each sensitized sample have been extrapolated from Tauc plots using the linear fitting procedure for direct band-gap semiconductors. (Table 1). A significant tail towards the infrared range – after the absorption edge of the considered materials – is observed for all samples and it is mainly due to the scattering properties of the TiO_2 scaffold. Although this feature is useful to increase the light path length through the device and thus the overall absorption, also results in some light lost during the optical measurements due to the enhanced back and lateral scattering.

# of CdS cycles	Estimated band-gap
4	2.54 ± 0.01 eV
8	2.47 ± 0.05 eV
12	2.45 ± 0.04 eV
16	2.43 ± 0.05 eV

Table 1 - Energy band-gap as a function of the number of CdS sensitization cycles, estimated from the Tauc plots of the absorptance spectra.

Photoelectrochemical characterization

Electrochemical performances of the samples are assessed through linear sweep voltammetry (LSV) curves and incident photon to current efficiency (IPCE), that corresponds to the external quantum efficiency (EQE) in the field of photovoltaics. The analysis is performed by varying both the amount of the CdS sensitization cycles and the thickness of the TiO_2 scaffold, in order to find the best performing device. LSV curves for TiO_2 scaffolds – sharing a common thickness of 5 µm – with increasing numbers of sensitization cycles (Figure 7 left) show a maximum photocurrent value of 3.8 $mA \cdot cm^{-2}$ for the 8-cycles sample, a better slope efficiency in the low-voltage range for the 4-cycles sample and a general degradation of performances for the more sensitized samples. This experimental trend can be explained by the concomitant effects arising from the thickness growth of the CdS layer. Thin films of CdS present a strong quantum confinement effect that broadens the optical band-gap of the material, thus providing a narrower range of absorption. On the other hand, the broadening of the CdS band-gap raises its conduction band with respect to the TiO_2 conduction band, thus providing more driving force to inject electrons in the supporting scaffold. Thin films present low optical densities and thus lack the ability to saturate the absorption near the band-edge. However, a low film thickness provides a lower rate of electron-hole recombination caused by defects as the photogenerated charges has to travel less through the material. Overall, increasing the CdS film thickness causes a deterioration in charge transport and charge injection, whereas it promotes an improvement in optical absorption and charge generation. In terms of photoelectrochemical performances, these opposing factors balance out in the optimal value of 8 sensitization cycles, where the photocurrent density is maximized. The 4-cycle sample exhibits a better fill-factor despite the lower saturation photocurrent, as the thin CdS layer efficiently inject the photogenerated charges in the supporting scaffold, but suffer from a reduced optical density. The dramatic decrease in performance shown by the 16-cycles sample is further explained with the complete clogging of the TiO_2 scaffold porosity caused by the thick CdS film deposited. The IPCE curves of these samples (Figure 7 right) further confirm the physical explanation previously reported concerning the quantum confinement effect on the optical band-gap. The 4-cycle sample with a thin CdS layer achieve IPCE values as high as 57%, but it can absorb just up to 490 nm due to its broadened band-gap, whereas the 16-cycles sample with a thick CdS layer absorbs light up to the quasi-bulk value of 504 nm, but has a maximum IPCE value of 32%. The integral of the IPCE curves over the wavelength range is equal to the photocurrent density values at 0.2 V_{RHE} (corresponding to the bias applied during the IPCE measurements) and the presented results are in good accordance with those provided by the LSV curves.

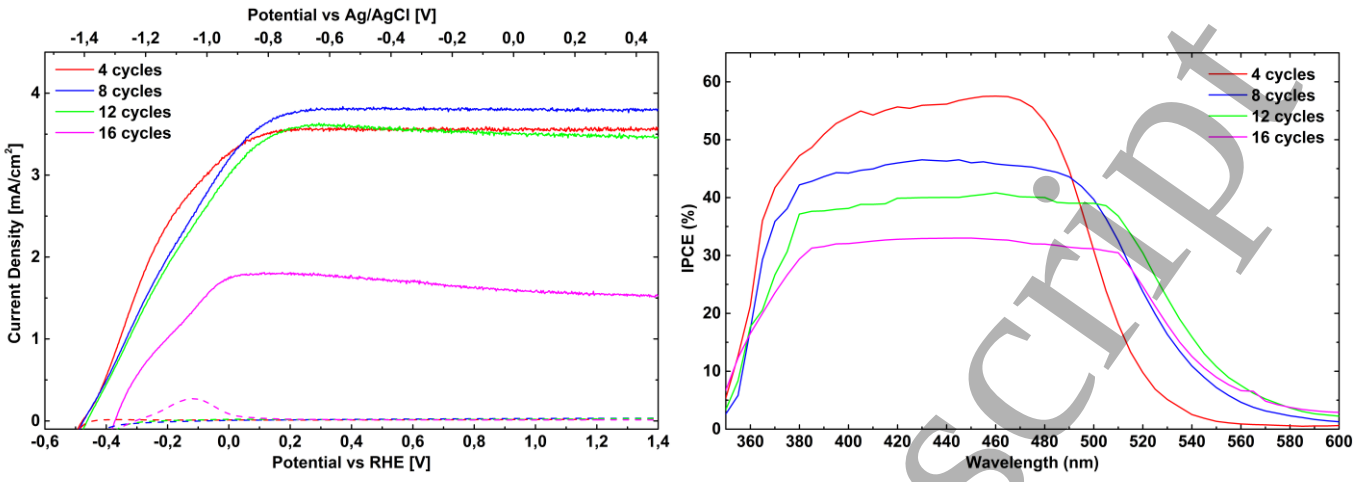

Figure 7 - LSV curves (left) and IPCE spectra collected at 0.2 V_{RHE} (right) of the 5-µm-thick TiO_2 scaffolds with increasing numbers of CdS sensitization cycles.

Electrochemical measurements are thence performed on samples with an increasing thickness of the TiO_2 scaffold, keeping the amount of sensitization to the optimal value of 8 cycles. The samples measured range from a scaffold thickness of 1 µm to 20 µm, including a 10 µm sample made of TiO_2 nanoparticle paste employed as a reference. As the thickness of the nano-trees grows, the effective surface area of the scaffold increases, thus allowing for a higher amount of CdS sensitizer to be deposited. In this way it is possible to improve the optical density of the whole device while keeping the thickness of the sensitization layer fixed at its optimized value, avoiding the detrimental effect of high charge recombination in thick films of CdS. In fact, the photocurrent values shown in the LSV curves (Figure 8 left) increase as the scaffold thickness grows, reaching a maximum of 6.6 $mA \cdot cm^{-2}$ for the 20 µm sample, with the effect of increased optical density already saturating the absorption for the 15-µm-thick sample. As a benchmark for performances, the reference TiO_2 nanoparticle paste sample provides photocurrent values consistently lower than its PLD-deposited counterpart of the same thickness. This result is attributed to the high amount of grain boundaries between nanoparticles and to the high defectivity of the nanocrystals that result in a strong increase of the electron-hole recombination rates. On the other hand, the quasi-1D hyperbranched morphology obtained with the optimized PLD technique benefits from strong directional growth and high degrees of crystallinity, which provide efficient transport pathways and low recombination rates for the photogenerated charges. The IPCE curves (Figure 8 right) on those samples reflect the performance trend highlighted by the LSV measurements, with the external conversion efficiency increasing with scaffold thickness and reaching a maximum value of 67% for the 20-µm sample.

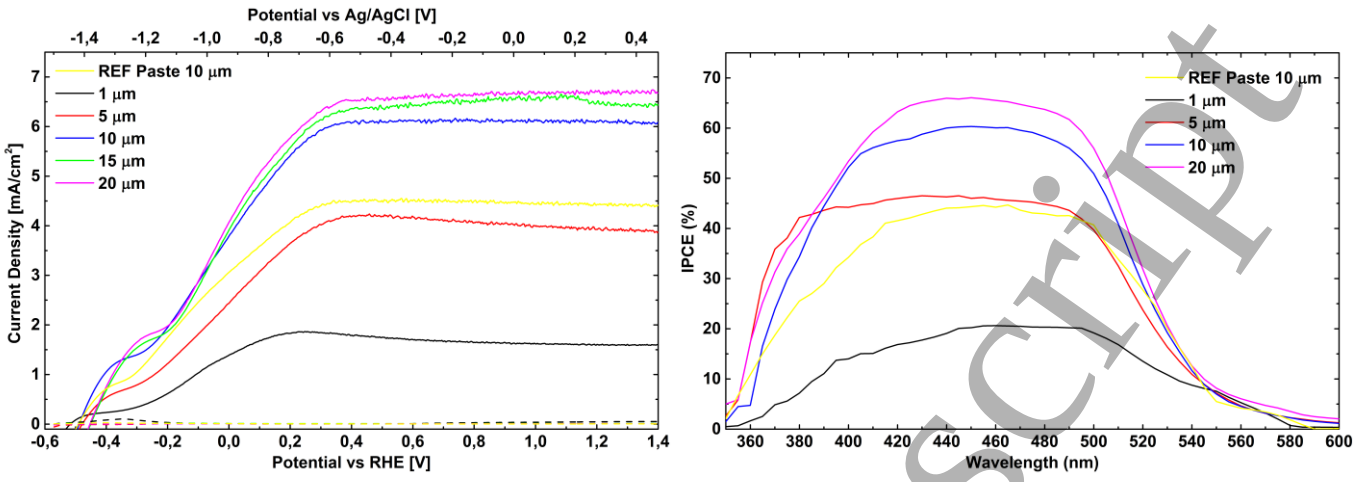

Figure 8 - LSV curves (left) and IPCE spectra collected at 0.2 V_{RHE} (right) of TiO_2 scaffolds with increasing thickness with 8 CdS sensitization cycles.

To confirm the claim of improved charge injection properties for thin layers of CdS, electrochemical impedance spectroscopy (EIS) is performed on all the samples and the electron lifetime is extracted from the obtained Bode plots (Figure S1). The frequency f_{max} of the characteristic peak in the Bode plots is correlated to electron lifetime τ_n according to the following relation:

$$\tau_n = \frac{1}{2\pi f_{max}}$$

For samples with increasing number of sensitization cycles the electron lifetime values shift from approximately 179 µs for the 8-cycles sample to 82 µs for the 16-cycles sample. As previously suggested as an explanation to the trend in LSV and IPCE curves, thicker CdS films suffer from higher rates of charge recombination caused by the intrinsic defectivity of the amorphous sensitizing material. Concurrently, samples with a different thickness of the TiO_2 scaffold show similar values of electron lifetime. This implies that the charge transport properties of the heterostructure are not hindered by the thickness of the TiO_2 scaffold, since the main limiting factor is the phenomenon of charge injection at the absorber/scaffold interface.

An important parameter to evaluate the performances of a PEC device is the ratiometric power-saved Φ_{saved},[65] which is defined as the advantage of employing an active photoelectrode to drive a given water-splitting half-reaction instead of an ideal, non-polarizable, dark electrode. The ratiometric power-saved Φ_{saved} is calculated as the difference between the ideal dark electrode voltage V_{dark} of 1.23 eV and the sweeping photoelectrode voltage V_{ph}, multiplied by the photocurrent density J_{ph} at each given photoelectrode voltage, divided by the incident illumination power density P_{sun}.

$$\Phi_{saved} = \frac{(V_{dark} - V_{ph}) \cdot J_{ph}}{P_{sun}}$$

The ratiometric power-saved (Figure S2) show how the peak value – called maximum power point – for each device is placed close to the zero potential at approximately around 0.2 VRHE, thanks to the efficient electron injection from CdS layer and thanks to the high electron injection mobility within the hyperbranched TiO2 scaffold that allow for high values

of photocurrent without the need of additional external driving force. The best performing device – the 20-µm TiO_2 scaffold with 8 cycles of CdS sensitization – achieves a ratiometric power-saved of 6% with an external bias of 0.2 V_{RHE} and a value of 5% at 0 V_{RHE}.

Another important benchmark of the internal charge injection and transport properties of a given device is the absorbed-photon-to-current efficiency (APCE) – obtained as the ratio between the IPCE and the absorptance of a sample and corresponding to the internal quantum efficiency (IQE) in the field of photovoltaics – that describes the internal conversion efficiency of the device to turn any absorbed photon into separated charges in the external circuit. The best performing device shows APCE values up to 90% within its range of absorption up to values of 500 nm, very close to the band-edge cut-off (Figure 9). This performance implies that absorbed photons are converted into photogenerated electron-hole pairs in the CdS photoactive layer, separated by the favorable energy level alignment, injected at the CdS/TiO_2 interface and then transported along the supporting scaffold, all the processes occurring efficiently thanks to the low recombination rates within the optimized thickness of the CdS layer and to the enhanced crystallinity and directionality of the hyperbranched TiO_2. Essentially, this optimized heterostructure nearly converts all the absorbed photons into electric charges to be employed in the process of hydrogen production.

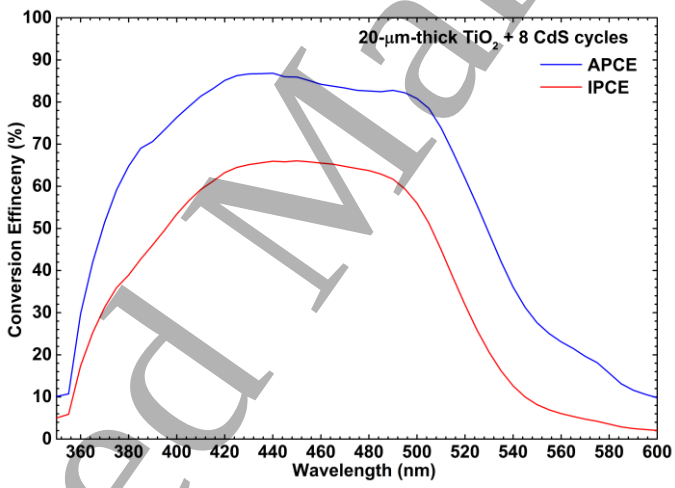

Figure 9 - APCE (blue) and IPCE (red) spectra collected at 0.2 V_{RHE} of the record sample, corresponding to the 20-um-thick TiO_2 scaffold with 8 CdS sensitization cycles.

To better understand these benchmark parameters, the optimized architecture presented in this work is compared with other state-of-the-art TiO_2/CdS photoanodes taken from the literature (Table 2). The performance comparison considers the photocurrent density under an applied bias of 0 V_{RHE} and the ratiometric power-saved at the maximum power point. In the perspective of a tandem PEC architecture, a steep photocurrent profile with an early onset potential plays a much more important role than a high saturation photocurrent achieved under strong positive applied biases. A similar reasoning can be made for the maximum power point where the ratiometric power-saved is calculated, as it represents the applied potential where the device best performs in terms of efficiency.

Photoelectrode	Electrolyte	Reference electrode	J_{PH} @ 0 V_{RHE}	Φ_{saved} @ MPP	Ref.
TiO_2 hyperbranched nano-trees + CdS conformal coating	0.25 M Na_2S + 0.35 M Na_2SO_3	Saturated silver-silver chloride (Ag/AgCl/sat. KCl)	4.06 mA·cm^{-2}	6.0 % @ 0.20 V_{RHE}	This work
TiO_2 micro-nanoporous film + CdS nanocrystals in the pores	0.2 M Na_2S + 1 M Na_2SO_3	Saturated mercury-mercurous sulfate (Hg/Hg_2SO_4/sat. K_2SO_4)	1.67 mA·cm^{-2}	5.2 % @ 0.32 V_{RHE}	Guo et al.[43]
TiO_2 nanorods + CdS conformal coating	0.25 M Na_2S + 0.35 M Na_2SO_3	Saturated silver-silver chloride (Ag/AgCl/sat. KCl)	2.80 mA·cm^{-2}	4.8 % @ 0.25 V_{RHE}	Luo et al.[47]
TiO_2 nanotubes + CdS quantum-dots	1 M Na_2S	Saturated silver-silver chloride (Ag/AgCl/sat. KCl)	3.48 mA·cm^{-2}	4.6 % @ 0.14 V_{RHE}	Chen et al.[45]

Table 2 - Performances for some of the best-performing TiO_2/CdS photoelectrodes for PEC water-splitting present in literature. Important details of the experimental conditions are also reported.

Regarding the photocurrent yield (Figure S3 left), most of the presented photoanodes achieve a maximum photocurrent density around 6 mA·cm^{-2} that corresponds to an external conversion efficiency around 80% at saturation, considering the theoretical Shockley–Queisser limit for a CdS absorbing layer of approximately 7.5 mA·cm^{-2}. An important distinction between the compared architectures appears on the photocurrent density achieved under 0 V_{RHE} of external bias, where our optimized photoanode achieves a value of 4.06 mA·cm^{-2}, clearly outperforming the other devices. The steep photocurrent profile of our photoanode translates into a high ratiometric power-saved value of 6%, obtained at the maximum power point of 0.2 V_{RHE}. Once again, these values are better than the reported devices (Figure S3 right) that present lower efficiencies and high maximum power point voltages. As thoroughly reported in this section, these performances are achieved thanks to the optimized hyperbranched TiO_2 scaffold and CdS absorption layer that efficiently absorb, inject and transport the photogenerated carriers.

Conclusions

The heterostructures comprising quasi 1D-hyperbranched TiO_2 nanostructured scaffolds sensitized with thin CdS films have proven to be efficient photoanodes for the production of hydrogen via solar energy. The mesoporous nano-tree morphology presents an elevated effective area and allows for an effective sensitization of its whole surface with a homogeneous layer of photoactive material, reaching high values of optical density even with low CdS thicknesses. Furthermore, the high internal scattering of the nano-trees increases the light-harvesting properties of the whole device by lengthening the path photons have to travel within the film. Efficient charge generation and injection of CdS film, thanks to the nanometric thickness and the resulting low recombination rates, are coupled with the improved charge transport properties of the scaffold, granted by the quasi-1D directional growth and the high crystallinity of the hyperbranched morphology. Thanks to these features, the best-performing device displays an onset potential of -0.43 V_{RHE}, a photocurrent density of 4.06 mA·cm^{-2} at 0 V_{RHE} and a saturation photocurrent density of 6.6 mA·cm^{-2} at 0.35 V_{RHE} with an internal conversion efficiency up to 90%. These figures of merit currently represent the state-of-the-art for TiO_2/CdS heterostructures for water-spitting applications, especially in the range of low external bias. According to

literature, higher performances are only achieved by exploiting chalcogenides with a lower optical band-gap, such as CdTe and CdSe, in order to drastically increase photon absorption and charge generation. A possible future development of this work could employ a TiO_2/CdS/CdSe type-II triple-material heterostructure, combining a better exploitation of the solar spectrum provided by the dual absorber with the efficient charge transport properties inherent to the nanostructured scaffold, thus theoretically pushing the photocurrent densities in the range of 20 $mA \cdot cm^{-2}$.[66–69] In general, thanks to the fine control over the morphology of the scaffold and to the versatility of the SILAR sensitization technique, future works might be focused on the development of a nano-heterostructures comprising hyperbranched TiO_2 nano-tree scaffold sensitized with a wide range of novel, yet to be investigated, photoactive materials.

Acknowledgement

Alessandro Mezzetti and Mehrdad Balandeh fabricated the devices and performed the overall characterization. Jingshan Luo and Chuawei Cheng helped in the SILAR sensitization process. Sebastiano Bellani helped in the impedance spectroscopy analysis. Alessandra Tacca and Laura Meda helped in the electrochemical characterization. Giorgio Divitini and Caterina Ducati performed the TEM analysis. Fabio Di Fonzo performed the SEM analysis. Fabio Di Fonzo and Honhjin Fan planned and supervised the whole work. All authors contributed to the interpretation of the results for the paper draft, written by Alessandro Mezzetti.

List of references

[1] Pinaud B A, Benck J D, Seitz L C, Forman A J, Chen Z, Deutsch T G, James B D, Baum K N, Baum G N, Ardo S, Wang H, Miller E and Jaramillo T F 2013 Technical and economic feasibility of centralized facilities for solar hydrogen production via photocatalysis and photoelectrochemistry *Energy Environ. Sci.* **6** 1983

[2] Fujishima A and Honda K 1972 Electrochemical Photolysis of Water at a Semiconductor Electrode *Nature* **238** 37–8

[3] Kavan L and Grätzel M 1995 Highly efficient semiconducting TiO2 photoelectrodes prepared by aerosol pyrolysis *Electrochim. Acta* **40** 643–52

[4] Fujishima A, Rao T and Tryk D 2000 Titanium dioxide photocatalysis *J. Photochem. Photobiol. C Photochem. Rev.* **1** 1–21

[5] Khan S U M, Al-Shahry M and Ingler W B 2002 Efficient photochemical water splitting by a chemically modified n-TiO2. *Science* **297** 2243–5

[6] Kitano M, Matsuoka M, Ueshima M and Anpo M 2007 Recent developments in titanium oxide-based photocatalysts *Appl. Catal. A Gen.* **325** 1–14

[7] Ni M, Leung M K H, Leung D Y C and Sumathy K 2007 A review and recent developments in photocatalytic water-splitting using TiO2 for hydrogen production *Renew. Sustain. Energy Rev.* **11** 401–25

[8] Fujishima A, Zhang X and Tryk D 2008 TiO2 photocatalysis and related surface phenomena *Surf. Sci. Rep.* **63** 515–82

[9] Valdés A, Qu Z, Kroes G, Rossmeisl J and Nørskov J 2008 Oxidation and photo-oxidation of water on TiO2 surface *J. Phys.*

Chem. C **2** 9872–9

[10] Mizukoshi Y and Masahashi N 2010 Photocatalytic activities and crystal structures of titanium dioxide by anodization: their dependence upon current density *Mater. Trans.* **51** 1443–8

[11] Nam W, Oh S, Joo H, Sarp S, Cho J, Nam B-W and Yoon J 2010 Preparation of anodized TiO2 photoanode for photoelectrochemical hydrogen production using natural seawater *Sol. Energy Mater. Sol. Cells* **94** 1809–15

[12] Chen X and Mao S S 2007 Titanium dioxide nanomaterials: synthesis, properties, modifications, and applications. *Chem. Rev.* **107** 2891–959

[13] Yun H J, Lee H, Joo J B, Kim N D and Yi J 2011 Effect of TiO2 Nanoparticle Shape on Hydrogen Evolution via Water Splitting *J. Nanosci. Nanotechnol.* **11** 1688–91

[14] Hou J, Yang X, Lv X, Huang M, Wang Q and Wang J 2012 Controlled synthesis of TiO2 mesoporous microspheres via chemical vapor deposition *J. Alloys Compd.* **511** 202–8

[15] Chiarello G L, Selli E and Forni L 2008 Photocatalytic hydrogen production over flame spray pyrolysis-synthesised TiO2 and Au/TiO2 *Appl. Catal. B Environ.* **84** 332–9

[16] Feng X, Shankar K, Varghese O K, Paulose M, Latempa T J and Grimes C a 2008 Vertically aligned single crystal TiO2 nanowire arrays grown directly on transparent conducting oxide coated glass: synthesis details and applications. *Nano Lett.* **8** 3781–6

[17] Liu Z, Pesic B, Raja K S, Rangaraju R R and Misra M 2009 Hydrogen generation under sunlight by self ordered TiO2 nanotube arrays *Int. J. Hydrogen Energy* **34** 3250–7

[18] Zhang Z, Hossain M F and Takahashi T 2010 Photoelectrochemical water splitting on highly smooth and ordered TiO2 nanotube arrays for hydrogen generation *Int. J. Hydrogen Energy* **35** 8528–35

[19] Wang G, Wang H, Ling Y, Tang Y, Yang X, Fitzmorris R C, Wang C, Zhang J Z and Li Y 2011 Hydrogen-treated TiO2 nanowire arrays for photoelectrochemical water splitting. *Nano Lett.* **11** 3026–33

[20] Mor G K, Kim S, Paulose M, Varghese O K, Shankar K, Basham J and Grimes C a 2009 Visible to near-infrared light harvesting in TiO2 nanotube array-P3HT based heterojunction solar cells. *Nano Lett.* **9** 4250–7

[21] Hardcastle F 2011 Raman Spectroscopy of Titania (TiO2) Nanotubular Water-Splitting Catalysts *J. Ark. Acad. Sci.* **65** 43–8

[22] Di Fonzo F, Casari C S, Russo V, Brunella M F, Li Bassi A and Bottani C E 2009 Hierarchically organized nanostructured TiO 2 for photocatalysis applications *Nanotechnology* **20** 15604

[23] Sauvage F, Di Fonzo F, Li Bassi A, Casari C S, Russo V, Divitini G, Ducati C, Bottani C E, Comte P and Graetzel M 2010 Hierarchical TiO 2 Photoanode for Dye-Sensitized Solar Cells *Nano Lett.* **10** 2562–7

[24] Buonsanti R and Carlino E 2011 Hyperbranched Anatase TiO2 Nanocrystals: Nonaqueous Synthesis, Growth Mechanism,

and Exploitation in Dye-Sensitized Solar Cells *J. Am. Chem. Soc.* **133** 19216–39

[25] Asahi R 2001 Visible-Light Photocatalysis in Nitrogen-Doped Titanium Oxides *Science (80-.).* **293** 269–71

[26] Lindgren T, Mwabora J M, Avendaño E, Jonsson J, Hoel A, Granqvist C-G and Lindquist S-E 2003 Photoelectrochemical and Optical Properties of Nitrogen Doped Titanium Dioxide Films Prepared by Reactive DC Magnetron Sputtering *J. Phys. Chem. B* **107** 5709–16

[27] Morikawa T, Asahi R and Ohwaki T 2005 Visible-light photocatalyst-nitrogen-doped titanium dioxide *R&D Rev. Toyota CRDL* **40** 45–50

[28] Valentin C Di, Pacchioni G and Selloni A 2005 Theory of carbon doping of titanium dioxide *Chem. Mater.* 6656–65

[29] Park J H J, Kim S and Bard A J A 2006 Novel carbon-doped TiO2 nanotube arrays with high aspect ratios for efficient solar water splitting *Nano Lett.* **6** 24–8

[30] Colon G, Maicu M, Hidalgo M C and Navio J 2006 Cu-doped TiO2 systems with improved photocatalytic activity *Appl. Catal. B Environ.* **67** 41–51

[31] Giamello E, Livіraghi S and Paganini M 2007 N doped TiO2: theory and experiment *Chem. Phys.* **339** 44–56

[32] Zaleska A 2008 Doped-TiO2: A Review *Recent Patents Eng.* 157–64

[33] Dozzi M V and Selli E 2013 Doping TiO2 with p-block elements: Effects on photocatalytic activity *J. Photochem. Photobiol. C Photochem. Rev.* **14** 13–28

[34] Li C, Hu P, Meng H and Jiang Z 2016 Role of Sulfites in the Water Splitting Reaction *J. Solution Chem.* **45** 67–80

[35] Quang N D, Kim D, Hien T T, Kim D, Hong S-K and Kim C 2016 Three-Dimensional Hierarchical Structures of TiO 2 /CdS Branched Core-Shell Nanorods as a High-Performance Photoelectrochemical Cell Electrode for Hydrogen Production *J. Electrochem. Soc.* **163** H434–9

[36] Zhang H, Zhang D, Qin X and Cheng C 2015 Three-Dimensional CdS-Sensitized Sea Urchin Like TiO 2 -Ordered Arrays as Efficient Photoelectrochemical Anodes *J. Phys. Chem. C* **119** 27875–81

[37] Zhang X, Zeng M, Zhang J, Song A and Lin S 2016 Improving photoelectrochemical performance of highly-ordered TiO 2 nanotube arrays with cosensitization of PbS and CdS quantum dots *RSC Adv.* **6** 8118–26

[38] David S, Mahadik M A, Chung H S, Ryu J H and Jang J S 2017 Facile Hydrothermally Synthesized a Novel CdS Nanoflower/Rutile-TiO 2 Nanorod Heterojunction Photoanode Used for Photoelectrocatalytic Hydrogen Generation *ACS Sustain. Chem. Eng.* **5** 7537–48

[39] Xie Z, Liu X, Wang W, Wang X, Liu C, Xie Q, Li Z and Zhang Z 2015 Enhanced photoelectrochemical and photocatalytic performance of TiO2 nanorod arrays/CdS quantum dots by coating TiO2 through atomic layer deposition *Nano Energy* **11** 400–8

[40] Yu J, Gong C, Wu Z, Wu Y, Xiao W, Su Y, Sun L and Lin C 2015 Efficient visible light-induced photoelectrocatalytic hydrogen production using CdS sensitized TiO 2 nanorods on TiO 2 nanotube arrays *J. Mater. Chem. A* **3** 22218–26

[41] Wang H, Bai Y, Zhang H, Zhang Z, Li J and Guo L 2010 CdS Quantum Dots-Sensitized TiO 2 Nanorod Array on Transparent Conductive Glass Photoelectrodes *J. Phys. Chem. C* **114** 16451–5

[42] Bai J, Li J, Liu Y, Zhou B and Cai W 2010 A new glass substrate photoelectrocatalytic electrode for efficient visible-light hydrogen production: CdS sensitized TiO2 nanotube arrays *Appl. Catal. B Environ.* **95** 408–13

[43] Guo M, Wang L, Xia Y, Huang W and Li Z 2016 Enhanced photoelectrochemical properties of nano-CdS sensitized micro-nanoporous TiO 2 thin films from gas/liquid interface assembly *J. Alloys Compd.* **684** 616–23

[44] Krbal M, Prikryl J, Zazpe R, Sopha H and Macak J M 2017 CdS-coated TiO 2 nanotube layers: downscaling tube diameter towards efficient heterostructured photoelectrochemical conversion *Nanoscale* **9** 7755–9

[45] Chen C, Xie Y, Ali G, Yoo S H and Cho S O 2011 Improved conversion efficiency of CdS quantum dots-sensitized TiO2 nanotube array using ZnO energy barrier layer. *Nanotechnology* **22** 15202

[46] Li J, Hoffmann M W G, Shen H, Fabrega C, Prades J D, Andreu T, Hernandez-Ramirez F and Mathur S 2012 Enhanced photoelectrochemical activity of an excitonic staircase in CdS@TiO2 and CdS@anatase@rutile TiO2 heterostructures *J. Mater. Chem.* **22** 20472–6

[47] Luo J, Ma L, He T, Ng C F, Wang S, Sun H and Fan H J 2012 TiO 2 /(CdS, CdSe, CdSeS) Nanorod Heterostructures and Photoelectrochemical Properties *J. Phys. Chem. C* **116** 11956–63

[48] Yin Y, Jin Z and Hou F 2007 Enhanced solar water-splitting efficiency using core/sheath heterostructure CdS/TiO2 nanotube arrays. *Nanotechnology* **18** 495608

[49] Ding D, Zhou B, Liu S, Zhu G, Meng X, Yang J, Fu W and Yang H 2017 A facile approach for photoelectrochemical performance enhancement of CdS QD-sensitized TiO 2 via decorating {001} facet-exposed nano-polyhedrons onto nanotubes *RSC Adv.* **7** 36902–8

[50] Li J, Hoffmann M W G, Shen H, Fabrega C, Prades J D, Andreu T, Hernandez-Ramirez F and Mathur S 2012 Enhanced photoelectrochemical activity of an excitonic staircase in CdS@TiO2 and CdS@anatase@rutile TiO2 heterostructures *J. Mater. Chem.* **22** 20472

[51] Ali Z, Shakir I and Kang D J 2014 Highly efficient photoelectrochemical response by sea-urchin shaped ZnO/TiO 2 nano/micro hybrid heterostructures co-sensitized with CdS/CdSe *J. Mater. Chem. A* **2** 6474–9

[52] Biswas S, Hossain M F and Takahashi T 2008 Fabrication of Grätzel solar cell with TiO2/CdS bilayered photoelectrode *Thin Solid Films* **517** 1284–8

[53] Gao X-F, Sun W-T, Hu Z-D, Ai G, Zhang Y-L, Feng S, Li F and Peng L-M 2009 An Efficient Method To Form Heterojunction CdS/TiO 2 Photoelectrodes Using Highly Ordered TiO 2 Nanotube Array Films *J. Phys. Chem. C* **113** 20481–5

[54] Zhao D and Yang C-F 2016 Recent advances in the TiO 2 /CdS nanocomposite used for photocatalytic hydrogen production and quantum-dot-sensitized solar cells *Renew. Sustain. Energy Rev.* **54** 1048–59

[55] Sun W-T, Yu Y, Pan H-Y, Gao X-F, Chen Q and Peng L-M 2008 CdS Quantum Dots Sensitized TiO 2 Nanotube-Array Photoelectrodes *J. Am. Chem. Soc.* **130** 1124–5

[56] Wang X, Liu G, Wang L, Pan J, Lu G Q (Max) and Cheng H-M 2011 TiO2 films with oriented anatase {001} facets and their photoelectrochemical behavior as CdS nanoparticle sensitized photoanodes *J. Mater. Chem.* **21** 869

[57] Passoni L, Ghods F, Docampo P, Abrusci A, Martí-Rujas J, Ghidelli M, Divitini G, Ducati C, Binda M, Guarnera S, Li Bassi A, Casari C S, Snaith H J, Petrozza A and Di Fonzo F 2013 Hyperbranched Quasi-1D Nanostructures for Solid-State Dye-Sensitized Solar Cells *ACS Nano* **7** 10023–31

[58] Passoni L, Criante L, Fumagalli F, Scotognella F, Lanzani G, Fonzo F Di, Science N, Polimi T, Italiano I, Pascoli V G and Fisica D 2014 Self-Assembled Hierarchical Nanostructures for High Efficiency Porous Photonic Crystals *ACS Nano* 12167–74

[59] Balandeh M, Mezzetti A, Tacca A, Leonardi S, Marra G, Divitini G, Ducati C, Meda L and Di Fonzo F 2015 Quasi-1D hyperbranched WO 3 nanostructures for low-voltage photoelectrochemical water splitting *J. Mater. Chem. A* **3** 6110–7

[60] Di Fonzo F, Tonini D, Li Bassi A, Casari C S, Beghi M G, Bottani C E, Gastaldi D, Vena P and Contro R 2008 Growth regimes in pulsed laser deposition of aluminum oxide films *Appl. Phys. A* **93** 765–9

[61] Hardcastle F 2009 The structure of titanium oxide in titania (TiO2) photoactive water-splitting catalysts by raman spectroscopy *Proc. Electrost. Soc. Am. Annu. Meet.*

[62] Su C, Shao C and Liu Y 2011 Electrospun nanofibers of TiO2/CdS heteroarchitectures with enhanced photocatalytic activity by visible light. *J. Colloid Interface Sci.* **359** 220–7

[63] Mali S S, Desai S K, Dalavi D S, Betty C a, Bhosale P N and Patil P S 2011 CdS-sensitized TiO2 nanocorals: hydrothermal synthesis, characterization, application. *Photochem. Photobiol. Sci.* **10** 1652–8

[64] Kumar P, Saxena N, Chandra R, Gupta V, Agarwal A and Kanjilal D 2012 Nanotwinning and structural phase transition in CdS quantum dots *Nanoscale Res. Lett.* **7** 584

[65] Coridan R H, Nielander A C, Francis S a, McDowell M T, Dix V, Chatman S M and Lewis N S 2015 Methods for comparing the performance of energy-conversion systems for use in solar fuels and solar electricity generation *Energy Environ. Sci.* **8** 2886–901

[66] Yang L, McCue C, Zhang Q, Uchaker E, Mai Y and Cao G 2015 Highly efficient quantum dot-sensitized TiO 2 solar cells based on multilayered semiconductors (ZnSe/CdS/CdSe) *Nanoscale* **7** 3173–80

[67] Xu Y-F, Wu W-Q, Rao H-S, Chen H-Y, Kuang D-B and Su C-Y 2015 CdS/CdSe co-sensitized TiO2 nanowire-coated hollow Spheres exceeding 6% photovoltaic performance *Nano Energy* **11** 621–30

[68] Rao H-S, Wu W-Q, Liu Y, Xu Y-F, Chen B-X, Chen H-Y, Kuang D-B and Su C-Y 2014 CdS/CdSe co-sensitized vertically aligned

anatase TiO2 nanowire arrays for efficient solar cells *Nano Energy* **8** 1–8

[69] Wang S, Dong W, Fang X, Wu S, Tao R, Deng Z, Shao J, Hu L and Zhu J 2015 CdS and CdSe quantum dot co-sensitized nanocrystalline TiO2 electrode: Quantum dot distribution, thickness optimization, and the enhanced photovoltaic performance *J. Power Sources* **273** 645–53